JOURNAL OF SPACECRAFT AND ROCKETS
Vol. 47, No. 6, November–December 2010

Digital Still Snapshots of the Stardust Sample Return Capsule Entry

Paul F. Wercinski*
NASA Ames Research Center, Moffett Field, California 94035
and
Peter Jenniskens†
SETI Institute, Mountain View, California 94043

DOI: 10.2514/1.40248

The 15 January 2006 reentry of the Stardust Sample Return capsule was photographed from 11.2-km altitude onboard NASA's DC-8 Airborne Laboratory in a series of brief 1/320 s exposures with a Nikon D70 digital still camera. The entry was detected from 09:57:13.5 to 09:57:53.5 UTC. Other instruments have demonstrated that most of the observed broadband flux is due to gray body radiation from the hot surface of the thermal protection system, except in the very beginning when strong emission lines of zinc from an ablating paint layer contributed significantly to the blue band. The measured flux in the green band was used to measure the surface-averaged temperature variation during flight, and the corresponding flux in the blue and red bands were used to verify the expected wavelength dependence of the gray body emission.

Nomenclature

A	=	surface area, m^2
B_λ	=	blackbody intensity, $W/m^2/nm/sr$
c	=	speed of light, m/s
D	=	distance to the capsule, km
e	=	elevation, deg
F_λ	=	apparent flux detected at aircraft, $W/m^2/nm$
H	=	altitude, km
h	=	Planck constant, J s
I_λ	=	intensity, $W/m^2/nm/sr$
k	=	Boltzmann constant, J/K
k_e	=	extinction coefficient
M_v	=	visual magnitude with capsule at distance of 100 km
m	=	apparent magnitude
T	=	temperature, K
t	=	time, s
α	=	viewing angle between forward pointed direction of capsule and direction to aircraft, deg
ε	=	emissivity
θ	=	angle normal to emitting surface, deg
λ	=	wavelength, nm
Ω	=	solid angle, sr

I. Introduction

THE Stardust Sample Return Capsule (SRC) reentered the Earth's atmosphere at a fast 12.8 km/s on 15 January 2006 [1]. The reentry was of significant technical importance because it was the fastest reentry ever made of a manmade object. Much of the phenomena associated with such fast reentries are poorly understood. Moreover, the Thermal Protection System (TPS) of the capsule was made of a Phenol Impregnated Carbon Ablator (PICA) and this reentry would be the first system field test of PICA under these conditions. Unfortunately, the Stardust entry vehicle was not instrumented to provide data about heating of the TPS. Consequently the only way to reconstruct the heating experienced by the Stardust entry vehicle was either through dissecting the recovered vehicle TPS or from observing the light emitted by the vehicle during reentry.

This paper presents broadband photometric data from the observation of the vehicle during reentry. It was predicted (and later confirmed by other instruments) that the radiation would be dominated by gray body emission from the hot surface along most of the entry trajectory [2,3]. In that case, surface temperature can be measured with simple imaging cameras equipped with broadband filters. The color filters in a digital still camera provided a means of doing broadband photometry of three colors, defined by the response of the blue, green, and red filters. Digital still photography proved of value during the Genesis Sample Return Capsule entry on 8 September 2004. At that time, we obtained broadband photometric measurements for about 11 s during the later part of the entry path. From that, it was concluded that the heat shield cooled slower than derived from models that did not include the thermal latency in the cooling of the nonablating TPS [4]. During the Stardust reentry observing campaign, the same camera and lens were used. The results proved of value in verifying the flux calibration of other camera systems, and to measure the surface-averaged temperature of the capsule's heat shield during entry.

II. Methods

The digital stills were taken with a hand-held Nikon D70 digital camera with 75–300 mm f/4.5–5.6 Nikon zoom lens set at focal length 250 mm and F-number f5.6. All Stardust entry images were taken at 1/320-s exposure, with the camera set at ISO 1600, and data recorded in raw format (Nikon Electronic image Format, or NEF) and Color Mode IIIa (sRGB) JPG files, with white balance set to AUTO. The settings did not change during the observations, with the camera operations set at manual (lesson learned from the Genesis reentry) [3]. The observer was positioned behind a standard acrylic DC-8 aircraft window in one of the emergency exit doors, at station L730. The response of the window is gray over the wavelength range covered here.

Received 5 August 2008; revision received 26 April 2009; accepted for publication 29 April 2009.

*Senior Staff Scientist, Space Technology Division, Mail Stop 230-2; Paul.F.Wercinski@nasa.gov. Member AIAA.

†Research Scientist, Carl Sagan Center, 515 N. Whisman Road; Petrus.M.Jenniskens@nasa.gov. Member AIAA.

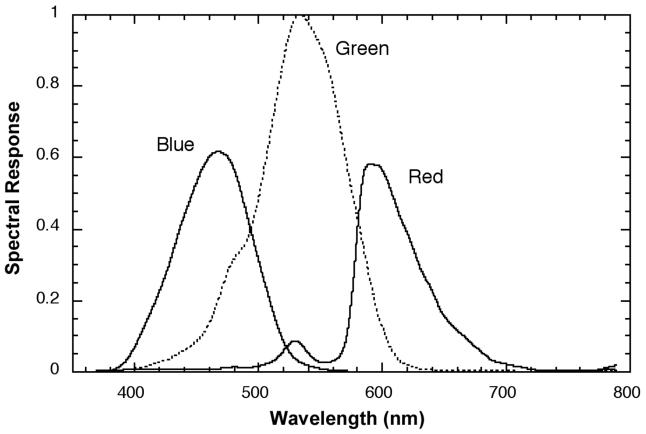

Fig. 1 Response curves for blue, green, and red fields of a Nikon D70 and 180 mm f2.8 Nikon lens (after Bui).

The camera uses a SONY ICX413 AQ CCD detector with image format 3040×2014 pixels of 7.8-micron size. The factory provided gain at ISO 400 setting is 2.57 electrons per ADU. The rms noise at ISO 400 is 13 electrons. The dynamic range is 12 bit (4095 ADU).

Christian Bui[‡] measured the relative spectral response curves for the Nikon D70 blue, green, and red filters of this commercial camera (Fig. 1). These are broadband filters with significant overlap, but sufficient separation in the response to be able to use the three-color response for color determinations. The position of the average response curve weighted wavelength in these graphs was used in our analysis (Table 1).

Absolute calibration was achieved using an astronomical source, the planet Mars. At 09:41:46.5 and 48.5 UMT, two exposures were taken with the same camera setting of the planet, then relatively low on the horizon. The number of measurements is unfortunately small because at the time of the measurement, Mars was not apparent on the camera's LCD screen. Only later it was discovered that these measurements could provide a useful calibration.

Five hours before the reentry, a GPS clock was photographed, showing that the exchangeable image file format (EXIF) time stamp is 5.5 ± 0.5 s earlier than the actual time of exposure.

III. Determination of the Responsivity of the Camera

Exposures of the SRC entry were taken from 09:57:07.5 to 09:58:02.5 UMT (Fig. 1). Most of the images came at 1-s intervals, but in a few places there was a 2 or 3 s gap. The capsule was detected on frames taken between 09:57:12.5 and 09:57:54.5 UMT. The capsule is not resolved in these images, but variations in color and intensity are obvious. The original images are 3008×2000 pixels in size. Figure 2 shows the cropped regions centered on the capsule.

Each image is slightly out of focus, the red fields more so than the blue fields. This is a mostly due to a combination of distortions in the window and lens chromatic aberration and defocus, with some contribution from atmospheric seeing. The aircraft window consisted of at least three acrylic panes that were slightly deformed.

Two images of Mars taken just before the SRC entry (Fig. 3) were used to calibrate the responsivity of the camera, translating the digital counts to an engineering unit (irradiance). The spectrum of Mars is to first order that of a G2V star, our Sun. The planet is a point source for this instrument, just like the SRC. The two images of Mars show the planet just barely detected. At the time of the exposures, the aircraft was at latitude $+39.78°$N, longitude $114.60°$W and altitude 11.72 km. The JPL/Horizons software gives the following position for Mars. Mars' apparent location was at R.A. = 2h49m46.7s, Decl = $+18°05'11''$ in the constellation Aries at a distance of 0.904 AU, in the general azimuth direction as the reentry. Mars' apparent visual magnitude was -0.20 magnitude above the atmosphere, when it was unresolved at $10.36''$ in diameter. The imaging scale of the camera was $9.5''$/pixel.

Mars was only $1.894°$ above the horizon (airmass 18.6), so that the atmospheric extinction was considerable. Clouds or high altitude haze were not apparent in intensified video of the scene. Using MODTRAN, we calculated extinction curves as a function of wavelength (350–900 nm) and found that to first order the extinction is an exponential function of airmass: $F/F_o = 1.0 * \exp(-k_e * \text{airmass})$ at this aircraft altitude, with coefficient $k_e = 0.0528$ at 548 nm (Table 1). From that, we calculated an extinction factor $F/F_o = 0.375$ for 548 nm, with F_o the extinction free apparent flux. Extinction included, the apparent visual magnitude of Mars was $m_v = +0.87$ magn.

Here, we use the astronomical unit of apparent magnitude, which is an irradiance, i.e., incident flux per unit area (= flux density). A ratio of irradiance (F_1/F_2) relates to magnitudes as: $\Delta m = -2.5 \log(F_1/F_2)$. Units of irradiance are $\mathrm{W/m^2(/nm)}$. Translation to absolute magnitude, a measure of radiance, i.e., flux density per unit solid angle, demands information about the distance to the source. In meteor astronomy, absolute magnitudes are defined for a normalized distance of 100 km. Radiometric units of radiance are $\mathrm{W\,m^{-2}\,ster^{-1}(/nm)}$.

The zero point for the magnitude scale varies with wavelength. In comparison with astronomical sources, we will use the calibration for a zero magnitude A0V standard listed in Table 1 [5].

The response curve weighted mean wavelength of the Nikon D70's B* (465.5 nm), G* (532.3 nm), and R* (604.2 nm) bands of Fig. 1 are slightly different from the Johnson bands, and we used interpolated values to take this into account (Table 1). The corresponding blue-, green-, and red-band magnitudes of Mars (including extinction) were: $B^* = +1.42$, $G^* = +0.93$, and $R^* = +0.85$ magn.

We subsequently extracted from each raw NEF image (Mars and SRC) the blue, green, and red fields, keeping the full 12-bit dynamic range, but extracting as an 8-bit image. Then we summed the pixel brightness values of each image, integrated over the source (after background subtraction). The measured B, G, and R band pixel brightness values for SRC and astronomical source were compared, and calibrated with the known magnitude of Mars, then translated into units of $\mathrm{W/m^{-2}/nm}$ using the zero point values to obtain the measured flux (F_λ). After subtracting a mean background derived from nearby pixels, the sum of pixel intensity was measured. All Mars and SRC images were near the center of the picture, so that no flatfield correction was needed. For Mars, we had: $\langle \Sigma B \rangle = 987 \pm 234$, $\langle \Sigma G \rangle = 1141 \pm 88$, $\langle \Sigma R \rangle = 1036 \pm 233$ ADU. This translated to a response of $6.4 \pm 1.5 \times 10^{13}$, $6.7 \pm 0.5 \times 10^{13}$ and $8.2 \pm 1.8 \times 10^{13}$ ADU per $\mathrm{W/m^2/nm}$ for B, G, and R band, respectively.

These values are specific to the neutral NEF colors and will change when working with color modes (as for our Genesis SRC entry observations). NEF files have a linear intensity scale per band. As a result, the calibration factors do not significantly differ from one band to the next, with the value for the Green band being the most reliable on account of containing twice the number of samples per pixel. We found that the green band is not only less noisy, but also contains less nonrandom structure. Based on that, we adopted a response of $6.7 \pm 0.5 \times 10^{13}$ ADU per $\mathrm{W/m^2/nm}$ for all bands.

Using the determined responsivity of the camera system, the observed flux values are listed in Table 2. The error bar was estimated based on the 1-sigma uncertainty in the background, corresponding to 0.90 ADU/pixel in the red band, 0.15 ADU/pixel in the green band and 0.97 ADU/pixel in the blue band. The (random) error in Table 2 does not include the $\geq 7\%$ systematic error from the calibration on Mars.

The result is plotted in Fig. 4. Error bars are the random error only. The red flux is usually higher than the green and blue flux, in agreement with most of the emission originating from a gray body continuum with color temperature <4000 K. For reasons probably related to hand tracking and window distortions, individual measurements jump on occasion (e.g., at 09:57:20.5 UMT).

[‡]For more information visit http://www.astrosurf.com/buil/d70v10d/eval.htm [retrieved September 2004].

Table 1 Adopted zero-point flux for magnitudes for Johnson UBVRI filters and Nikon D70 filters. Extinction coefficients $k_e(\lambda)$ are integrated over passband

Nikon	Johnson:	λ, nm weight	peak	FWHM[a] nm	F_λ for 0 magnitude W/m^{-2}/nm	$k_e(\lambda)$ /airmass
	B	444.3		83.1	6.40×10^{-11}	0.0600
	V	548.3		82.7	3.67×10^{-11}	0.0528
	R	685.5		174.2	1.92×10^{-11}	0.0259
	I	863.7		197.0	9.39×10^{-12}	0.0069
B*		465.5	468	83	5.71×10^{-11}	0.0526
G*		532.3	533	75	3.99×10^{-11}	0.0516
R*		604.2	591	60	2.76×10^{-11}	0.0588

[a]Full width at half maximum.

The digital still camera provided one of several independent flux calibrations. In particular, there is good agreement with flux measurements at 548 nm measured by the echelle-based spectrograph for the crisp and high efficient detection of low light emission, called ECHELLE (Fig. 4, open squares) [6]. This is a validation of the absolute calibration on Mars.

In the early period from 09:57:13.5 to 19.5 UMT, the blue band emission is stronger than the green band emission. This is the period when strong atomic lines of Zinc were observed by other instruments, which radiate in the blue band.

Peak heating was expected to occur at around 09:57:33 UMT, at the time when our images are saturated. It is noticeable, however, that the fluxes are indicative of a higher temperature around 09:57:30 as compared with 09:57:50, when the capsule started to cool off.

IV. Discussion

A. Surface Temperature

The observed irradiance can be translated into radiance by dividing by the solid angle subtended by the surface area of the SRC as seen from the observer $\Delta\Omega = A/D^2$ steradian, where A is the projected surface area (in m^2) and D the distance to the SRC (in m). The corresponding measure of radiance can be used to determine the surface brightness temperature if the emission is dominated by a blackbody continuum. The radiance of a black body is described by the Planck function

$$B_\lambda(T) = 2hc^2/\lambda^5 * 1/[\exp(hc/\lambda kT) - 1] \quad (1)$$

which describes how much radiation energy is traveling through a differential surface δA at an angle θ to the normal of that area into a differential solid angle $\delta\Omega$, per unit of time t and per unit of wavelength λ. In which case, with λ in units of nm, the average surface temperature follows from

$$T(K) = 1.4388379 \times 10^7/\lambda/(\ell_n(1.0 + 1.191071 \times 10^{20}/(\lambda^5 I_\lambda))) \quad (2)$$

with $I_\lambda = F_\lambda/(A/D^2)/\varepsilon$. The projected surface area of the shield is $A = 0.52$ m^2 when viewed face-on and smaller if the viewing angle α increases. We adopted the projected surface area for different viewing angles ($\alpha = 0°$, normal to the front) listed in Table 3.

The material emissivity (ε) for the Stardust SRC heat shield (the ratio of the emitted intensity to the Planck function) is not known to us, but can be measured from the recovered shield. Literature values for various carbon materials give values ranging from 0.73 to 0.97. We adopt $\varepsilon = 0.88$, independent of wavelength (gray body). Other constants used include the speed of light, $c = 2.99793 \times 10^8$ m/s;

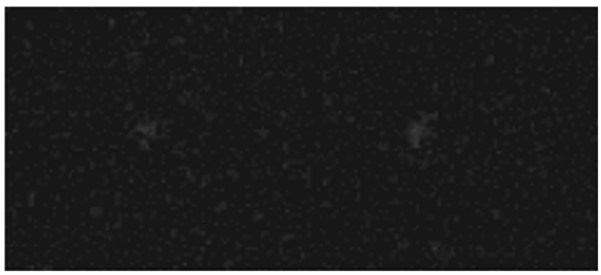

Fig. 3 Two unresolved images of Mars, contrast and brightness enhanced, with same camera setting at 09:41:46.5 + 48.5 UMT.

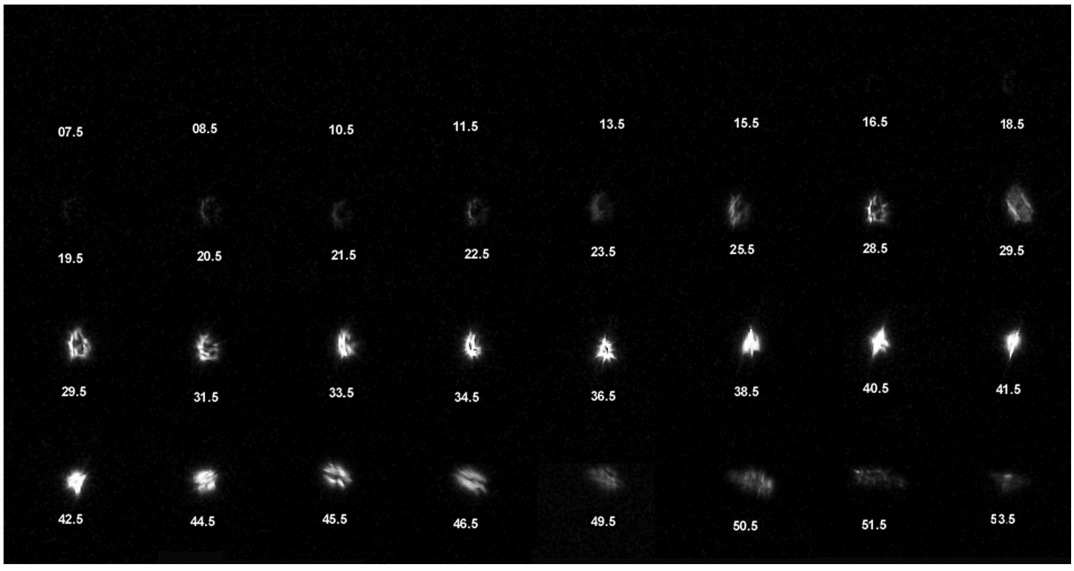

Fig. 2 Cropped digital images of the Stardust Sample Return Capsule entry. Distortions are due to scattering from atmospheric seeing, aircraft window, and camera optics. Times are uncertain by ±0.5 s.

Table 2 Apparent flux of SRC entry, just outside of aircraft window, corrected for extinction in line of sight. *H* is the altitude of the capsule, *e* is the elevation above the horizon, *D* is the range from capsule to aircraft, F_λ is the measured flux, and *Mv* is the magnitude of the source as seen from a distance of 100 km

UTC 09:57	*H* km	*D* km	*e* °	F/F_o 532 nm	F_λ (blue) W/m²/nm		F_λ (green) W/m²/nm		F_λ (red) W/m²/nm		*Mv* magn.
13.5	87.6	459.6	7.1	0.678	5.6e − 11	±2.0e − 11	6.0e − 12	±2.7e − 12	8.6e − 12	±1.6e − 11	+1.9
14.5	86.0	447.4	7.2	0.682	——	——	——	——	——	——	——
15.5	84.5	435.2	7.3	0.686	2.9e − 11	2.6e − 11	1.3e − 11	3.4e − 12	2.3e − 11	1.8e − 11	+1.0
16.5	82.9	422.9	7.4	0.690	3.4e − 11	1.0e − 11	1.7e − 11	1.9e − 12	2.6e − 11	1.4e − 11	+0.8
17.5	81.4	410.6	7.5	0.694	——	——	——	——	——	——	——
18.5	80.0	398.3	7.7	0.699	5.1e − 11	1.4e − 11	5.2e − 11	2.5e − 12	9.2e − 11	1.7e − 11	−0.5
19.5	78.5	386.1	7.9	0.704	6.4e − 11	2.0e − 11	6.3e − 11	3.4e − 12	1.3e − 10	2.7e − 11	−0.7
20.5	77.1	373.9	8.1	0.709	1.6e − 10	2.0e − 11	2.1e − 10	2.7e − 12	3.2e − 10	2.9e − 11	−1.9
21.5	75.7	361.8	8.3	0.714	1.4e − 10	1.6e − 11	2.0e − 10	3.1e − 12	2.6e − 10	2.2e − 11	−1.9
22.5	74.4	349.7	8.5	0.720	2.1e − 10	1.9e − 11	3.1e − 10	2.8e − 12	4.2e − 10	2.0e − 11	−2.4
23.5	73.1	337.7	8.7	0.726	2.6e − 10	2.8e − 11	3.8e − 10	3.5e − 12	4.9e − 10	2.7e − 11	−2.6
24.5	71.8	325.8	9.0	0.732	——	——	——	——	——	——	——
25.5	70.6	314.0	9.2	0.738	5.9e − 10	2.5e − 11	7.0e − 10	3.9e − 12	1.0e − 09	3.6e − 11	−3.3
26.5	69.4	302.4	9.5	0.744	5.7e − 10	2.5e − 11	9.1e − 10	3.5e − 12	1.3e − 09	3.3e − 11	−3.5
27.5	68.2	290.9	9.8	0.750	——	——	——	——	——	——	——
28.5	67.0	279.5	10.1	0.756	8.8e − 10	3.2e − 11	1.2e − 09	6.2e − 12	1.8e − 09	5.6e − 11	−3.8
29.5	65.9	268.4	10.5	0.762	1.0e − 09	3.8e − 11	1.5*e* − 09	5.0e − 12	2.2e − 09	5.0e − 11	−4.1
30.5	64.9	257.4	10.8	0.769	——	——	——	——	——	——	——
31.5	63.8	246.6	11.2	0.775	[saturated]						
32.5	62.8	236.0	11.6	0.781	——	——	——	——	——	——	——
33.5	61.9	225.6	12.0	0.787	[saturated]						
34.5	60.9	215.5	12.5	0.793	[saturated]						
35.5	60.1	205.6	12.9	0.799	——	——	——	——	——	——	——
36.5	59.2	196.0	13.4	0.805	[saturated]						
37.5	58.4	186.7	13.9	0.811	——	——	——	——	——	——	——
38.5	57.6	177.6	14.4	0.816	[saturated]						
39.5	56.9	168.9	15.0	0.822	——	——	——	——	——	——	——
40.5	56.1	160.4	15.5	0.827	[saturated]						
41.5	55.5	152.3	16.1	0.832	[saturated]						
42.5	54.8	144.5	16.7	0.837	[saturated]						
43.5	54.2	137.1	17.4	0.842	——	——	——	——	——	——	——
44.5	53.6	130.0	18.0	0.847	1.1e − 09	6.8e − 11	1.4e − 09	5.9e − 12	2.2e − 09	3.8e − 11	−4.0
45.5	53.1	123.3	18.7	0.852	7.5e − 10	2.7e − 11	1.1e − 09	6.2e − 12	1.9e − 09	4.1e − 11	−3.8
46.5	52.5	116.9	19.4	0.857	7.1e − 10	3.7e − 11	1.2e − 09	4.9e − 12	1.9e − 09	4.5e − 11	−3.8
47.5	52.1	111.0	20.2	0.861	——	——	——	——	——	——	——
48.5	51.6	105.4	20.9	0.865	——	——	——	——	——	——	——
49.5	51.2	100.3	21.7	0.869	5.1e − 10	3.9e − 11	8.8e − 10	4.6e − 12	1.4e − 09	4.1e − 11	−3.5
50.5	50.7	95.5	22.6	0.873	4.1e − 10	3.3e − 11	8.3e − 10	5.9e − 12	1.3e − 09	3.9e − 11	−3.5
51.5	50.4	91.2	23.4	0.877	2.0e − 10	4.2e − 11	4.6e − 10	4.1e − 12	7.7e − 10	4.1e − 11	−2.8
52.5	50.0	87.4	24.3	0.881	——	——	——	——	——	-.-	-.-
53.5	49.7	84.0	25.2	0.885	1.7e − 10	3.2e − 11	3.4e − 10	4.5e − 12	5.9e − 10	4.0e − 11	−2.5

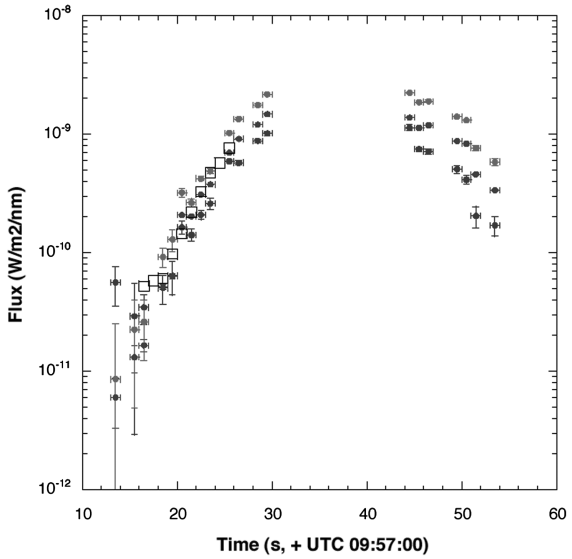

Fig. 4 Apparent flux in the three camera filters. Blue, green, and red symbols indicate the blue, green, and red pass bands. Open squares are measurements at 548 nm obtained by a miniature slitless ECHELLE spectrograph [6].

the Planck constant $h = 6.62620 \times 10^{-34}$ J s; and Boltzmann's constant $k = 1.38062 \times 10^{-23}$ J/K.

The assumption that the surface temperature is constant over the projected area is naive. A more careful analysis is presented elsewhere [7]. The results presented here merely serve to judge the relative flux measured in the blue, green, and red fields of our camera. Equation (1) defines how the expected flux varies as a function of wavelength. The calculated ratio is that for the central wavelengths of each band. The observed values include the response from a wider (partially overlapping) pass band (Fig. 1) and the observed ratios tend to be slightly smaller. Again, the zinc line emission is clearly detected in the blue band early during the reentry.

B. Resolved Image of Stardust Entry

Of particular interest is the speckled appearance of the images. One bright speckle at 09:52:5 UMT is particularly interesting, enlarged in Fig. 5, because it has a red glow just left of it.

It is likely that this red glow is due to wavelength-dependent image distortions by the multipaned and not perfectly plane-parallel acrylic aircraft window, as a similar red halo is seen in other images shown in Fig. 2.

Alternatively, the red glow may represent the wake of the capsule if each speckle represents a separate image of the capsule. If so, the wake is observed to extend for about 20 m behind the capsule, and the

Table 3 Mean surface temperatures T, capable of producing the observed flux F_λ from a projected surface area A at a distance D (Table 2). The final four columns give the ratio of observed and calculated pixel intensities, based on the surface temperature derived from the measured intensity in the green band

UTC	F_λ(@D = 100 km)	A	I_λ	T	Green/blue		Red/green	
09:57	W/m^2/mm	m^2	W/m^2/nm/sr	K	calculated	observed	calculated	observed
13.5 ± 0.5	1.3e − 10	0.513	3.0	1929	3.8	0.1 ± 0.1	2.8	1.4 ± 2.8
15.5	2.7e − 10	0.511	6.0	2035	3.4	0.4 ± 0.4	2.6	1.7 ± 1.4
16.5	3.2e − 10	0.510	7.0	2060	3.4	0.5 ± 0.1	2.5	1.6 ± 0.9
18.5	9.0e − 10	0.509	20.0	2244	2.9	1.0 ± 0.3	2.2	1.8 ± 0.3
19.5	1.1e − 09	0.509	23.6	2277	2.8	1.0 ± 0.3	2.2	2.1 ± 0.4
20.5	3.1e − 09	0.508	69.0	2510	2.4	1.3 ± 0.2	1.9	1.5 ± 0.1
21.5	2.7e − 09	0.508	61.5	2483	2.4	1.4 ± 0.2	1.9	1.3 ± 0.1
22.5	4.0e − 09	0.507	88.6	2571	2.3	1.5 ± 0.1	1.9	1.4 ± 0.1
23.5	4.4e − 09	0.507	99.4	2601	2.3	1.4 ± 0.2	1.8	1.3 ± 0.1
25.5	7.3e − 09	0.506	163.0	2735	2.1	1.2 ± 0.1	1.7	1.5 ± 0.1
26.5	8.8e − 09	0.505	198.3	2792	2.1	1.6 ± 0.1	1.7	1.5 ± 0.1
28.5	9.9e − 09	0.503	224.1	2828	2.0	1.4 ± 0.1	1.7	1.5 ± 0.1
29.5	1.1e − 08	0.502	253.5	2866	2.0	1.5 ± 0.1	1.6	1.5 ± 0.1
			[Saturation]					
44.5	2.5e − 09	0.436	65.3	2497	2.4	1.2 ± 0.1	1.9	1.6 ± 0.1
45.5	1.9e − 09	0.426	49.4	2432	2.5	1.5 ± 0.1	2.0	1.6 ± 0.1
46.5	1.7e − 09	0.417	47.4	2423	2.5	1.7 ± 0.1	2.0	1.6 × 0.1
49.5	9.4e − 10	0.382	28.0	2311	2.7	1.7 ± 0.1	2.1	1.6 × 0.1
50.5	8.1e − 10	0.369	25.0	2288	2.8	2.0 ± 0.2	2.2	1.6 × 0.1
51.5	4.1e − 10	0.355	13.2	2167	3.1	2.2 ± 0.5	2.3	1.7 ± 0.1
53.5	2.6e − 10	0.324	9.0	2102	3.2	2.0 ± 0.4	2.5	1.7 ± 0.1

source of the red glow is likely the First Positive band emission of N_2. The capsule moved from left to right at the time of the exposure. The capsule was close to the observer at the time, only $D = 80$ km distant, and the scene was viewed from a large angle of 56° from the direction of motion of the capsule. The capsule was 26° above the horizon. The spatial scale is 3.7 m/pixel at this distance (Fig. 5), and the capsule itself remains unresolved.

Red color was also apparent in images by our ground team at Redding, California, where Bryan Murahashi of San José captured a back view of the reentry using a similar Nikon D70 with a 400 mm focal length lens, set at ISO = 800, with a 1/200 sec exposure at F/6.3 (Fig. 6). Again, the images appear slightly resolved, but now motion blurring from imperfect tracking may have contributed.

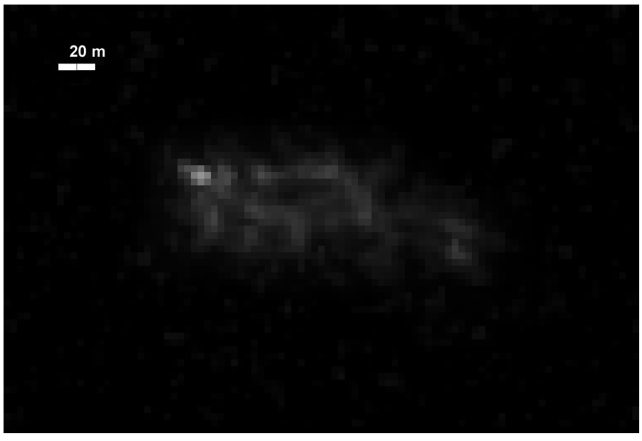

Fig. 5 Magnified image at 09:57:54.5 UMT. Scale bar represents 20 m at position of SRC.

V. Conclusions

Digital still images of the planet Mars, taken just minutes before the reentry of the Stardust Sample Return Capsule, provided an independent calibration of the apparent broadband flux during entry. The result agrees with independent flux estimates by the ECHELLE instrument. The present work extends the broadband flux measurements beyond the range of ECHELLE, and past the point of peak heating.

The flux measurements in the green band, combined with the projected surface area and the known distance to the capsule, provided a surface-averaged temperature of the hot heat shield over much of the entry path, except during peak heating when the signal was saturated. The expected wavelength-dependent emission in the blue and red bands were found consistent with those observed.

The spatial scale of the images was several meters per pixel at the distance to the capsule, and as a result the capsule was not resolved. Evidence for an extended red wake behind the capsule is not conclusive.

VI. Future Work

The results are available now for interpretation. The observations of the STARDUST Sample Return Capsule entry

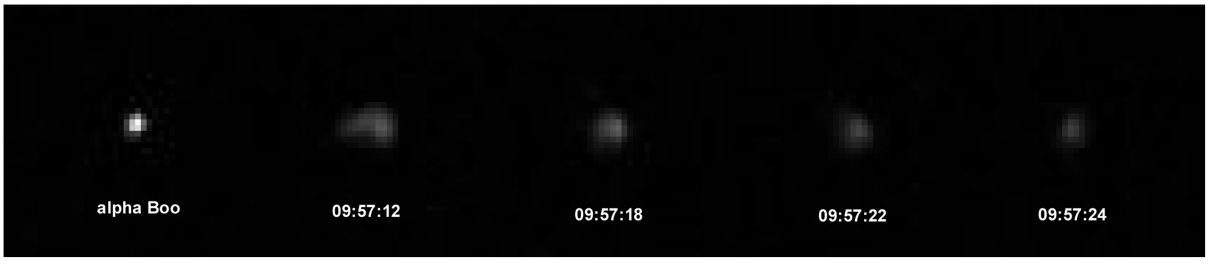

Fig. 6 Backview images of the Stardust SRC entry at 09:57 + 12 , 18, 22, and 24 s UMT by Bryan Murahashi from Redding, California. The white dot to the left is an image of the star alpha Bootes (a point source) taken just before the SRC observations.

are expected to remain a unique system field test for a long time to come. The observational data and the calibration files will be archived for this purpose. The present paper serves to document the files in hand.

Acknowledgments

We thank the ground-based observers that contributed to this article, in particular Bryan Murahashi of San José. NASA's DC-8 Airborne Laboratory was deployed by the University of North Dakota/National Suborbital Education and Research Center under contract with NASA Wallops Flight Center. This work was funded and managed by the Orion Thermal Protection System Advanced Development Project and the NASA Engineering and Safety Center.

References

[1] Desai, P. N., Lyons, D. T., Tooley, J., and Kangas, J., "Entry, Descent, and Landing Operations Analysis for the Stardust Re-Entry Capsule," *Presented at the 44th AIAA Aerospace Sciences Meeting and Exhibit*, AIAA Paper 2006-6410, Reno, NV, Jan. 2006.

[2] Jenniskens, P., Wercinski, P., Olejniczak, J., Raiche, G., Kontinos, D., Allen, G., Desai, P. N., Revelle, D., Hatton, J., Baker, R. L., Russell, R. W., Taylor, M., and Rietmeijer, F., "Preparing for Hyperseed MAC: An Observing Campaign to Monitor the Entry of the Genesis Sample Return Capsule," *Earth Moon and Planets*, Vol. 95, Nos. 1–4, 2006, pp. 339–360. doi:10.1007/s11038-005-9021-2

[3] Jenniskens, P., Wercinski, P., Spalding, D., Sandquist, K., Rossano, G., Russell, R. W., ReVelle, D., Hladiuk, D., and Hildebrand, A., "Technical Note: Status Report with Results from the 2004 Hyperseed MAC Genesis Campaign," Report to the NASA Engineering and Safety Center (NESC), NASA Ames Research Center, Internal Publication, 2004.

[4] Jenniskens, P., Kontinos, D., Jordan, D., Wright, M., Olejniczak J., Raiche, G., Wercinski, P., Desai, P. N., Taylor, M. J., Stenbaek-Nielsen, H. C., McHarg, M. G., Abe, S., Rairden, R. I., Albers, J., Winter, M., Harms, F., Wolf, J., ReVelle, D. O., Gural, P., Dantowitz, R., Rietmeijer, F., Hladiuk, D., and Hildebrand, A. R., "Preparing for the Meteoric Return of Stardust," SP-643, *Proc. Dust in Planetary Systems*, edited by A. Grapps, E. Gruen, ESA, The Netherlands, Sept. 2005.

[5] Colina, L., Bohlin, R., and Castelli, F., "Absolute Flux Calibrated Spectrum of Vega," Space Telescope Science Institute, Instrument Science Rept. CAL/SCS-008, 1996.

[6] Jenniskens, P., "Observations of the STARDUST Sample Return Capsule Entry with a Slit-less Echelle Spectrograph," AIAA, Paper 2008–1210Jan. 2008.

[7] Trumble, K. A., Cozmuta, I., Sepka, S., and Jenniskens, P., "Post-Flight Aerothermal Analysis of the Stardust Return Capsule," AIAA, Paper 2008–1210Jan. 2008.

M. Wright
Guest Editor